Applied Catalysis B: Environmental 309 (2022) 121210

Contents lists available at ScienceDirect

Applied Catalysis B: Environmental

journal homepage: www.elsevier.com/locate/apcatb

# Blue light photocatalysis of carbazole-based conjugated microporous polymers: Aerobic hydroxylation of phenylboronic acids to phenols

Xiaoyun Dong, Huimin Hao, Fulin Zhang, Xianjun Lang *

*Sauvage Center for Molecular Sciences and Hubei Key Lab on Organic and Polymeric Optoelectronic Materials, College of Chemistry and Molecular Sciences, Wuhan University, Wuhan 430072, China*

ARTICLE INFO

*Keywords:*
Conjugated microporous polymer
Carbazole
Aerobic hydroxylation
Phenylboronic acids
Blue light

ABSTRACT

Aerobic hydroxylation of phenylboronic acids to phenols has attracted considerable attention but is exceedingly challenging due to the obstacle in the activation of oxygen ($O_2$). Here, two carbazole-based conjugated microporous polymers (CMPs), namely TCB-CMP and EFC-CMP, were fabricated through polymerization of 1,3,5-tri(9*H*-carbazole-9-yl)benzene (TCB) and 9,9′-(9,9-diethyl-9*H*-fluorene-2,7-diyl)bis(9*H*-carbazole) (EFC), respectively. Gratifyingly, with *N,N′*-diisopropylethylamine (DIPEA) as the hole ($h^+$) quencher, blue light photocatalysis of both carbazole-based CMPs could execute the aerobic hydroxylation of phenylboronic acids in ethanol ($C_2H_5OH$). Importantly, the EFC-CMP imparted superior photocatalytic activity to TCB-CMP due to the favorable reduction of $O_2$ to superoxide anion ($O_2^{\bullet-}$) by electron ($e^-$). Thereby, $O_2^{\bullet-}$ conducted the highly selective aerobic hydroxylation of phenylboronic acids. The aerobic hydroxylation of a wide range of phenylboronic acids to corresponding phenols was achieved with high yields. The work further demonstrates the feasibility of taming the oxidation potential of CMPs in producing delicate products like phenols.

## 1. Introduction

Phenol and its derivatives are ubiquitous scaffolds in multitudinous intermediates and natural products [1–3]. Moreover, phenol and functionalized phenols have found pervasive application in manufacturing commodity polymers and producing high value pharmaceuticals, agrochemicals, and biologically active ingredients [4]. The direct hydroxylation of arene C–H is highly challenging [5,6]. However, the hydroxylation of arenes with a prefunctionalized site like aryl halides and phenylboronic acids becomes much more accessible. Nevertheless, many traditional methods for the aerobic hydroxylation of phenylboronic acids relied on noble transition metals [7] or strong stoichiometric oxidants such as oxone [8], organic peroxide, and hydrogen peroxide [9]. Alternatively, visible light photocatalysis for selective generation of functionalized phenols from aryl halides [10] or phenylboronic acids [11–13] with $O_2$ as the oxidant has attracted tremendous attention. However, challenge arises in the activation of $O_2$ into a variety of reactive oxygen species (ROS) from either $h^+$ or $e^-$ by semiconductor photocatalysis [14–22]. Both the substrate phenylboronic acids and the product phenols are delicate organic molecules that are susceptible to the attack of ROS. However, their oxidative potentials could be tamed by eliminating undesired ROS and promoting favorable one. Amongst the ROS, $O_2^{\bullet-}$ is one of the most suitable for the highly selective generation of phenols via the aerobic hydroxylation of phenylboronic acids [23], effectively evading the overoxidation of phenols.

$O_2^{\bullet-}$ could reign supreme provided that other ROS like hydroxyl radical ($^{\bullet}OH$) from either $h^+$ oxidation or $e^-$ reduction could be entirely eliminated. This could be feasible with $C_2H_5OH$ as the solvent [24]. In this scenario, the oxidative potential of $h^+$ should be tamed to circumvent the oxidation of $C_2H_5OH$. To date, there is no preceding report about the aerobic oxidation of aliphatic alcohols over organic semiconductor photocatalysts but is less uncommon over inorganic semiconductors. Intriguingly, the ROS could be regulated by different oxidation reactions over organic semiconductor photocatalysts [25–28]. Thus, organic semiconductors like CMPs could be a wise choice for organic reactions to proceed in $C_2H_5OH$ [29]. Distinctly, CMPs emerge as the new generation of organic semiconductor photocatalysts [30–40], owing to traits like strong optical absorption ability, abundance of building blocks, tunable band gaps and redox potentials, and excellent accessibility and robustness. A seminal report has accounted that oxidative coupling polymerization is a straightforward and efficient avenue to acquire carbazole-based CMPs [41]. Thereafter, carbazole

* Corresponding author.
*E-mail address:* xianjunlang@whu.edu.cn (X. Lang).

https://doi.org/10.1016/j.apcatb.2022.121210
Received 21 December 2021; Received in revised form 21 January 2022; Accepted 10 February 2022
Available online 12 February 2022

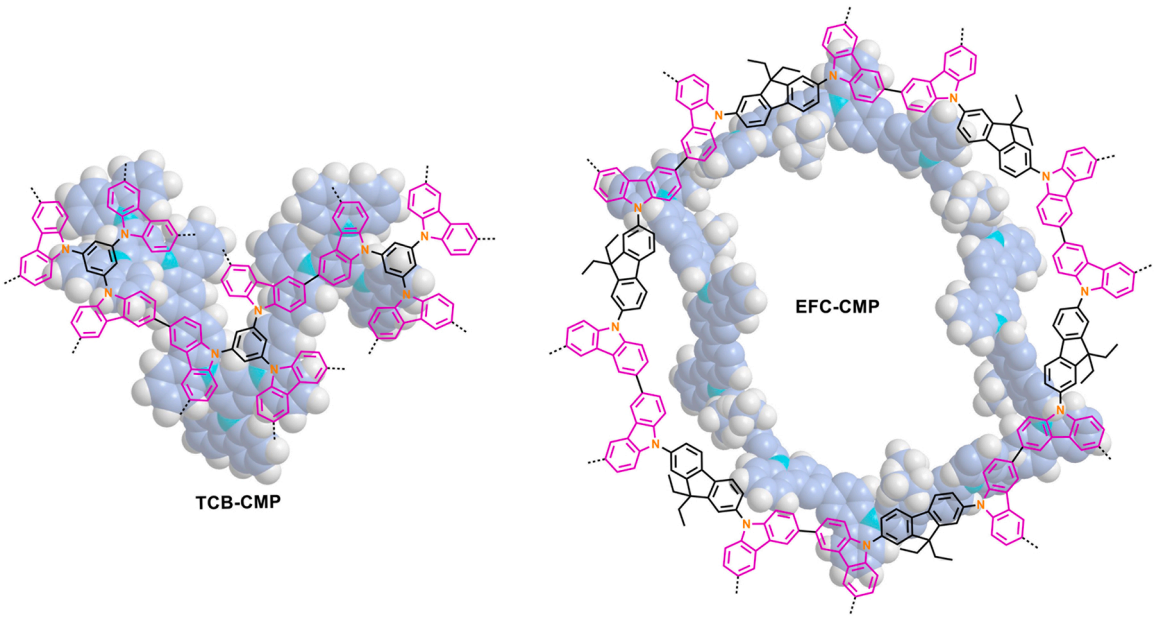


**Fig. 1.** Schematic illustration of carbazole-based CMPs of TCB-CMP and EFC-CMP.

with the rigid conjugated backbone featuring potential electron-donating capabilities and permanent porosity becomes the competitive building block [42–45]. Additionally, carbazole-based CMPs have abundant absorption towards the visible region on account of the distinct bathochromic shift feature capacitated by the extended π-conjugated segment of carbazole [46–50].

Hitherto, carbazole-based CMPs have found widespread applications in catalysis [51], contaminant removal [30,52], polymer films [53,54], electroluminescence [43], gas adsorption [52,55], and photocatalysis [56–59]. Besides, the fabrication of omnifarious carbazole-based CMPs have been reported, exhibiting impressive photocatalytic performances in which $O_2^{\bullet-}$ and $h^+$ worked in concert for the selective formation of imines and sulfoxides [60–62]. Here, carbazole acts as Lewis base to close the distance with the $–B(OH)_2$ group having an electron-deficient boron center as Lewis acid, promoting aerobic hydroxylation of phenylboronic acids [63]. Moreover, after losing $e^-$ for activating $O_2$ to $O_2^{\bullet-}$, $h^+$ is fully quenched by DIPEA rather than $C_2H_5OH$ and avoids the oxidation of functionalized phenols over carbazole-based CMPs.

Herein, two carbazole-based CMPs, namely TCB-CMP and EFC-CMP, were designed and fabricated through C–C coupling polymerization from TCB and EFC, respectively (Fig. 1). Owing to the significant C–H acidity of protons at $sp^3$ carbon, fluorene is very active under basic conditions, therefore the synthesis of 3,6-di(9*H*-carbazol-9-yl)− 9*H*-fluorene in which the 9*H* position of fluorene occupied by H remain elusive. Therefore, compared with TCB-CMP, 9,9-diethyl-9*H*-fluorene was envisaged as the electron acceptor for EFC-CMP. Gratifyingly, with DIPEA as the $h^+$ quencher, blue light photocatalysis of both carbazole-based CMPs could execute the selective aerobic hydroxylation of phenylboronic acids with $O_2$ in $C_2H_5OH$. In this process, carbazole establishes the potential of $h^+$. Then, $h^+$ could not be quenched by $C_2H_5OH$ but DIPEA, ensuring the highly selective generation of phenols. Importantly, EFC-CMP imparted superior photocatalytic activity to TCB-CMP due to favorable generation of $e^-$ in activating $O_2$ into $O_2^{\bullet-}$. Thereby, $O_2^{\bullet-}$ further conducted the highly selective hydroxylation of phenylboronic acids, alleviating the overoxidation of phenols. Meanwhile, aerobic hydroxylation of a wide range of phenylboronic acids to corresponding phenols was achieved with high yields. The work further demonstrates the feasibility of taming the oxidation potential of $h^+$ by selecting suitable building blocks of CMPs and regulating conditions in producing delicate products like phenols.

## 2. Experimental section

### 2.1. Preparation of 2-phenyl-1,3,2-dioxaborinane

Phenylboronic acid (1219.4 mg, 10.0 mmol), 1,3-propanediol (837.0 mg, 11.0 mmol), and dichloromethane ($CH_2Cl_2$, 10 mL) were charged into a 50 mL round-bottomed flask for stirring continuously at room temperature. And the transformation was monitored by thin-layer chromatography (TLC) until phenylboronic acid was completely consumed. Next, the crude mixture was dried over anhydrous $Na_2SO_4$, filtered, and evaporated to remove the solvent. After the purification by silica gel column chromatography (petroleum ether:dichloromethane = 5:1) and the concentration by rotary evaporation, the pure product of 2-phenyl-1,3,2-dioxaborinane (1603.8 mg, 99%) was ultimately afforded as a colorless oil.

### 2.2. Preparation of TCB-CMP and EFC-CMP

The TCB was purchased from TCI. The EFC was furnished via the Ullmann coupling between carbazole and 2,7-dibromo-9,9-diethyl-9*H*-fluorene. And the details for synthesis are described in the Supplementary data. The TCB-CMP and EFC-CMP were obtained by adopting the $FeCl_3$-induced C–C coupling polymerization.

And the preparation for TCB-CMP is elaborated as follows. Firstly, under nitrogen ($N_2$) protection, $FeCl_3$ (324.4 mg, 2.0 mmol) and anhydrous $CH_2Cl_2$ (20 mL) were charged in a round-bottomed flask. Afterward, anhydrous $CH_2Cl_2$ (20 mL) dissolving TCB (172 mg, 0.3 mmol) was added dropwise into the above mixture, running for 72 h at room temperature under the reflux condition. Then methanol ($CH_3OH$, 30 mL) was added to stir for 1 h for quenching the oxidative coupling polymerization. The crude product was filtered, washed with $CH_3OH$, and dispersed in concentrated hydrochloric acid (HCl, 30 mL) for stirring of another 1 h. After the suspension was filtered, the attained filter cake was washed with $H_2O$ and $CH_3OH$, then extracted in $CH_3OH$ and tetrahydrofuran (THF) in a Soxhlet extractor for 24 h, respectively. After drying in a vacuum chamber at 120 ℃ for 48 h, the product appeared as a light yellow powder (163.8 mg). Elemental analysis (%) calcd. for $(C_{42}H_{21}N_3)_n$: C 88.87, H 3.73, N 7.40; found: C 78.89, H 4.32, N 5.74.

Likewise, $FeCl_3$ (924.6 mg, 5.7 mmol), EFC (200.0 mg, 0.36 mmol), and anhydrous $CHCl_3$ (35 mL) were engaged in the polymerization at 60 °C for 72 h. Ultimately, the target EFC-CMP presented as a brown

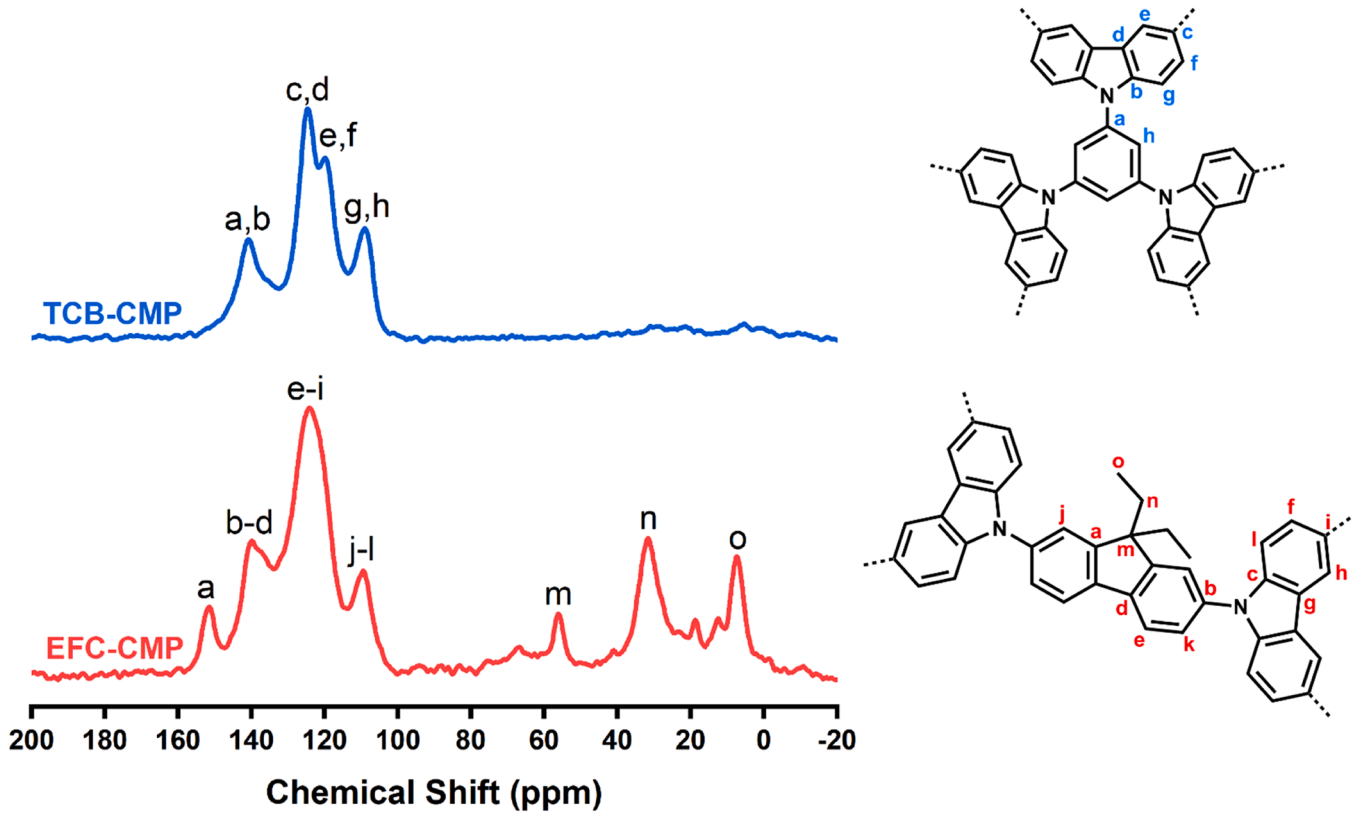


**Fig. 2.** Solid-state $^{13}C$ NMR spectra of TCB-CMP and EFC-CMP.

powder (199.3 mg). Elemental analysis (%) calcd. for $(C_{41}H_{28}N_2)_n$: C 89.75, H 5.14, N 5.11; found: C 74.74, H 5.49, N 3.39.

### 2.3. Typical procedure for aerobic hydroxylation reaction

At the outset, the photocatalyst (5 mg) was evenly dispersed in the mixed solution comprising of phenylboronic acid or 2-phenyl-1,3,2-dioxaborinane (0.6 mmol), DIPEA (3 mmol, 5.0 equiv.), and $C_2H_5OH$ (5 mL) in a 20 mL Pyrex reactor by ultrasonication for 5 min. Then the system went through stirring in the dark for 0.5 h to gain adsorption–desorption equilibrium. Next, the Pyrex reactor with a holed butyl rubber septum was placed in the magnetic stirring apparatus at 1500 rpm and irradiated by four sets of 3 W blue LED (3 W × 4). The supernatant dissociated by centrifugation was quantified by gas chromatography configured with a flame ionization detector (GC–FID). Ultimately, the products were identified by comparing the retention time of the authentic samples by GC–FID and further confirmed by gas chromatography–mass spectrometry (GC–MS).

## 3. Results and discussion

### 3.1. Characterizations for the two carbazole-based CMPs

In principle, carbazole could act as the site of Lewis base to close the distance with phenylboronic acids and donate $e^-$ for the generation of $O_2^{\bullet-}$, cooperatively promoting aerobic hydroxylation of phenylboronic acids. Thus, two carbazole-based monomers TCB and EFC were subjected to $FeCl_3$-induced C–C coupling polymerization to afford TCB-CMP

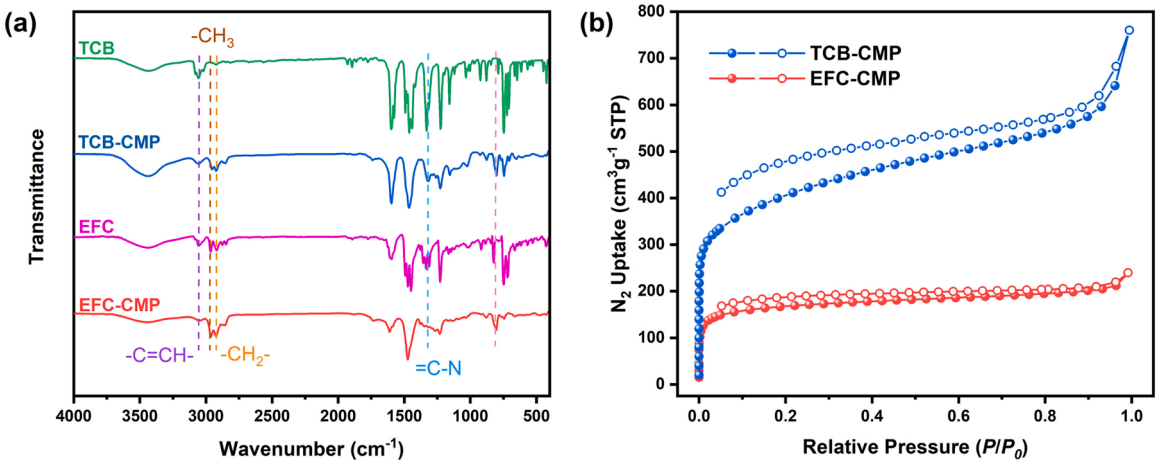


**Fig. 3.** (a) FTIR spectra of TCB-CMP, EFC-CMP, and corresponding monomers; (b) $N_2$ adsorption/desorption isotherms of TCB-CMP and EFC-CMP.

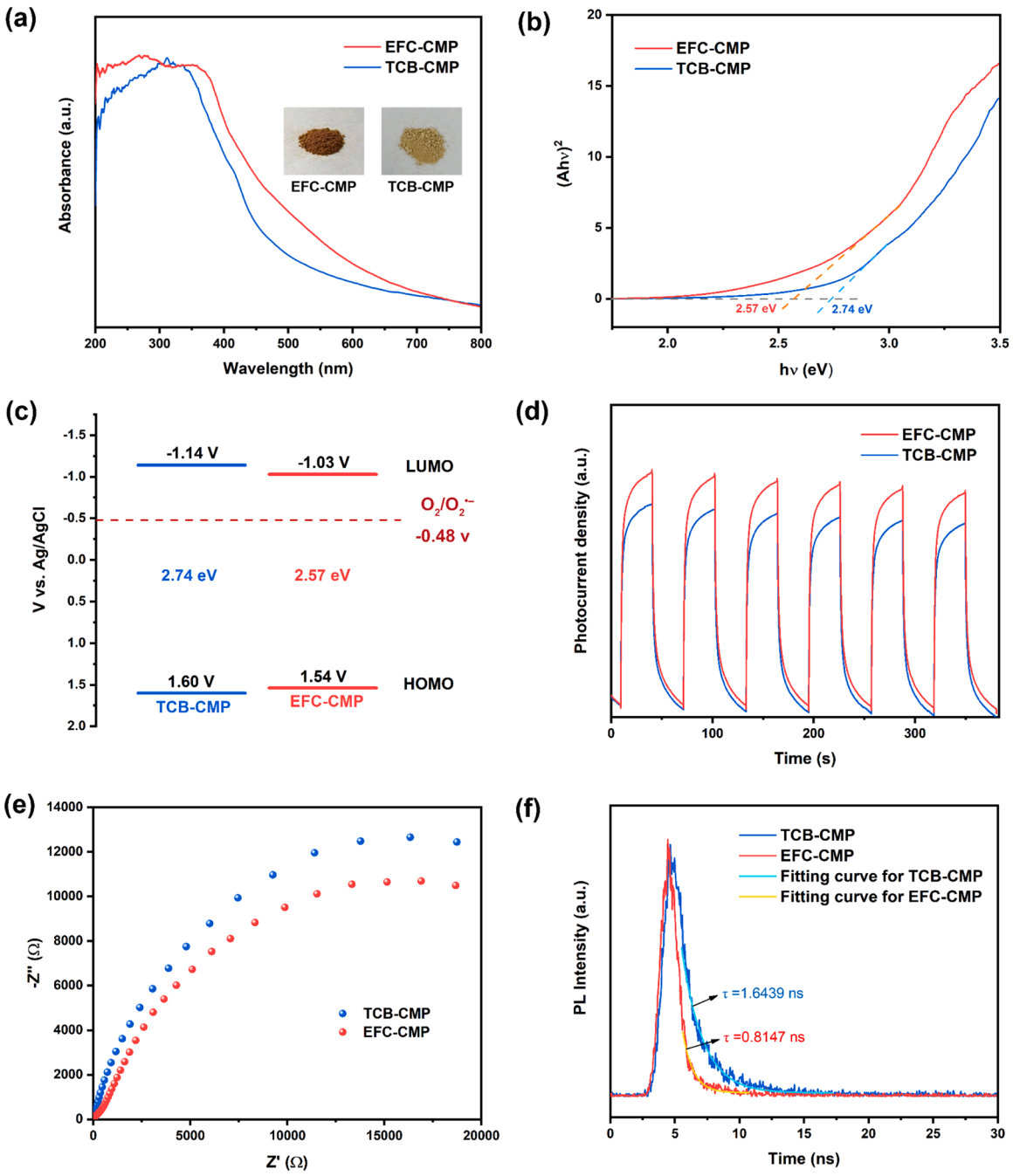


**Fig. 4.** (a) UV–vis DRS of TCB-CMP and EFC-CMP; (b) the Tauc plots of TCB-CMP and EFC-CMP; (c) electronic band structures of TCB-CMP and EFC-CMP; (d) transient photocurrent responses of TCB-CMP and EFC-CMP; (e) the Nyquist plots of EIS of TCB-CMP and EFC-CMP; and (f) TRPL spectra of TCB-CMP and EFC-CMP.

and EFC-CMP, respectively. The subsequent treatments of these two carbazole-based CMPs could exclude the effect of remaining Fe contents. The residual Fe contents in both carbazole-based CMPs (0.088 wt% for TCB-CMP and 0.086 wt% for EFC-CMP) were almost negligible, verified by inductively coupled plasma–atomic emission spectroscopy (ICP–AES). Besides, the obtained TCB-CMP and EFC-CMP are amorphous materials with hierarchical architectures, indicated by the high-resolution transmission electron microscopy (HRTEM) images (Supplementary Fig. S1) and the powder X-ray diffraction (PXRD) patterns (Supplementary Fig. S2). Meanwhile, TCB-CMP adopts a net-like morphology formed by stacking agglomerated nanospherical particles. While EFC-CMP appears a coral-like network structure proved by the field emission scanning electron microscopy (FE–SEM) (Supplementary Fig. S3). Additionally, the as-prepared carbazole-based CMPs possess high resistance to concentrated HCl, $H_2O$, and general organic solvents such as $CH_2Cl_2$, $CH_3OH$, and THF. As shown by thermogravimetric analysis (TGA) and differential thermogravimetric (DTG) curves (Supplementary Fig. S4), two apparent thermal decomposition behaviors were observed separately around 420 and 600 ℃ in an atmosphere of $N_2$, displaying favorable thermal endurance for TCB-CMP and EFC-CMP. Different from EFC-CMP, significant loss of weight occurred around 100 ℃ for TCB-CMP, which might be caused by solvent desorption in the porous structure of TCB-CMP. Meanwhile, TCB-CMP presents a slightly higher thermal stability with 85% weight maintenance up to about 600 ℃.

The chemical structures of TCB-CMP and EFC-CMP were assessed by the solid-state $^{13}C$ NMR and the Fourier-transform infrared (FTIR) spectroscopy. The resonances in the solid-state $^{13}C$ NMR spectra are

displayed in Fig. 2. As for TCB-CMP, the resonances at ca. 140.8 and 124.6 ppm correspond to the substituted phenyl carbons connecting with the nitrogen atom and the other substituted phenyl carbons, respectively. Moreover, the high-intensity peaks at ca. 119.5 and 109.0 ppm are ascribed to the unsubstituted phenyl carbons. While for EFC-CMP, the high-field signals at ca. 7.3 and 31.6 ppm are ascribed to the $sp^3$ carbon atoms in $–CH_3$ and $–CH_2–$ of 9,9-diethyl-9*H*-fluorene, respectively. Also, the chemical shift at ca. 55.9 ppm originates from the quaternary carbon bonded to the diethyl- group in 9,9-diethyl-9*H*-fluorene.

Meanwhile, the attribution of the peaks in the FTIR spectra has been present in Fig. 3a. Compared to TCB and EFC, the weakened intensity for the signal peak at ca. 3056 $cm^{-1}$ in the spectra of TCB-CMP and EFC-CMP is attributable to the disappearance of the C–H bond resulting from the connection of two phenyl carbons in the adjacent carbazoles. The phenomenon is indicative of the success of polymerization. According to an earlier report [60], the occurrence of the absorption band at ca. 805 $cm^{-1}$ belonging to the trisubstituted phenyl ring in carbazole validates the conclusion again. Also, the vibration of the C–N bond connecting carbazole and phenyl is located at ca. 1226 $cm^{-1}$. Besides, the fingerprint peaks centered at ca. 2960 and 2923 $cm^{-1}$ are assigned to the stretching vibration of $–CH_3$ and the antisymmetric stretching vibration of $–CH_2–$, respectively. As for EFC-CMP, the absorption peaks belong to the $–CH_3$ and $–CH_2–$ in 9,9-diethyl-9*H*-fluorene. Whereas for TCB-CMP, this may be caused by residual solvents such as $CH_3OH$ and THF. Moreover, most fingerprint peaks inherited from the monomers have been retained, admitting to conduct the ensuing investigations.

Besides, the intrinsic hierarchically porous traits of TCB-CMP and EFC-CMP were revealed by the $N_2$ adsorption/desorption isotherms at 77 K (Fig. 3b). The swift increase in adsorbate volume at the low $P/P_0$ region ($< 0.05$) in the $N_2$ adsorption isotherms could be observed, disclosing the presence of abundant micropores. While the mild increase for the $N_2$ uptake at $0.05 < P/P_0 < 1$ illustrates the permanent mesoporous architecture. Further, the architecture of TCB-CMP and EFC-CMP were confirmed by the pore size distribution following the nonlocal density functional theory (NLDFT) model (Supplementary Fig. S5). Also, TCB-CMP exhibits a relatively higher specific surface area of 1330 $m^2 g^{-1}$ and a larger pore volume of 0.95 $cm^3 g^{-1}$ based on the Brunauer–Emmett–Teller (BET) model, which is more than twice those of EFC-CMP with a BET specific surface area of 521 $m^2 g^{-1}$ and a pore volume of 0.32 $cm^3 g^{-1}$. But both carbazole-based CMPs appear the similar pore size, namely 5.1 nm for TCB-CMP and 5.3 nm for EFC-CMP. Notably, a larger specific surface area does not endow a better photocatalytic conversion of organic molecules because a large portion of micropores of CMPs is inaccessible for large molecules like phenylboronic acid and 2-phenyl-1,3,2-dioxaborinane.

The optical response ranges provide a powerful reference for understanding the inherent light-harvesting capacities of the as-prepared CMPs. Hence, the UV–visible diffuse reflectance spectroscopy (UV–vis DRS) was adopted to record the absorptance of TCB-CMP and EFC-CMP. Compared with TCB and EFC, a distinct extension effect for the light-absorption range of CMPs could be observed, exhibiting a bathochromic shift feature (Supplementary Fig. S6). Besides, both TCB-CMP and EFC-CMP disclose similar absorption bands ranging from 200 to 550 nm, which level off until the near-infrared region (Fig. 4a). Accordingly, the obtained TCB-CMP and EFC-CMP are deemed to have excellent light-responsive ability and effective absorbance for the visible-light region. Determined from Kubelka–Munk function with the Tauc plot method, the band gap values of TCB-CMP and EFC-CMP were estimated from the tangent intercepts of the plots as 2.74 and 2.57 eV based on the acquired UV–vis DRS (Fig. 4b).

The generation of ROS $O_2^{\bullet-}$ from $O_2$ is vital for the selective hydroxylation of phenylboronic acids. As a result, the Mott–Schottky plots of TCB-CMP and EFC-CMP were conducted to corroborate their redox potentials, revealing their semiconducting behaviors concurrently (Supplementary Fig. S7). Firstly, the positive slopes for the

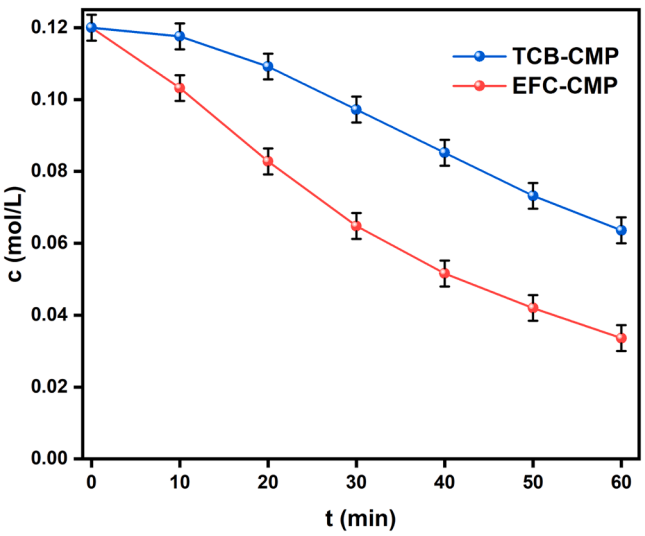


**Fig. 5.** Kinetic curves for aerobic hydroxylation of 2-phenyl-1,3,2-dioxaborinane to phenol by blue light photocatalysis of the carbazole-based CMPs. Reaction conditions: 2-phenyl-1,3,2-dioxaborinane (0.6 mmol), photocatalyst (5 mg), DIPEA (5.0 equiv.), blue LEDs ($\lambda = 460 \pm 10$ nm), $C_2H_5OH$ (5 mL), air (1 atm).

Mott–Schottky plots obtained at different frequencies unveil a feature of n-type semiconductor for TCB-CMP and EFC-CMP. Secondly, the flat-band potential ($E_{fb}$) of TCB-CMP and EFC-CMP are fitted to be −1.14 and −1.03 V vs. Ag/AgCl, respectively, estimated from the Mott-Schottky equation. Theoretically, the lowest unoccupied molecular orbital (LUMO) position generally approaches the $E_{fb}$ of the n-type semiconductor. Therefore, the corresponding LUMO values referring to the $E_{fb}$ were determined as −1.14 V for TCB-CMP, and −1.03 V for EFC-CMP, which are more negative than the potential of $O_2/O_2^{\bullet-}$ couple (–0.48 V vs. Ag/AgCl) to generate $O_2^{\bullet-}$ for implementing hydroxylation of phenylboronic acids. The highest occupied molecular orbital (HOMO) levels of TCB-CMP and EFC-CMP were estimated as +1.60 and +1.54 V vs. Ag/AgCl, respectively. The electronic structures of TCB-CMP and EFC-CMP and the reduction potential of $O_2/O_2^{\bullet-}$ are displayed in Fig. 4c.

Next, the separation efficiency and transfer characteristics of interfacial charges in CMPs were further explored by more elaborate electrochemical techniques. TCB-CMP and EFC-CMP both present speedy photocurrent responses, along with several reduplicative cycles during on/off irradiation (Fig. 4d). Compared with that of TCB-CMP, a stronger cathodic photocurrent signal of EFC-CMP was observed, elucidating the more excellent separation and higher electron mobility for photoinduced charge carriers. In line with electrochemical impedance spectroscopy (EIS), the smaller capacitance arc for EFC-CMP in the Nyquist plot indicates that EFC-CMP features lower transfer resistance and higher transfer efficiency for the interfacial charges (Fig. 4e). In addition, the linear sweep voltammetry (LSV) result further gives evidence for more efficient inhibition about recombination of photoinduced charge carriers in EFC-CMP than in TCB-CMP (Supplementary Fig. S8). This probably be caused by that TCB-CMP consists of benzene as a weak electron acceptor with carbazole as electron donor, giving rise to inhibit efficient separation and transfer of intramolecular charge carriers.

In comparison, the molecular underpinning of EFC-CMP contributes to a more efficient separation for photoinduced charge carriers within the networks. Nevertheless, the photoluminescence (PL) lifetime of TCB-CMP (1.64 ns) is twice as long as that of EFC-CMP (0.81 ns), as shown in the time-resolved photoluminescence (TRPL) spectra (Fig. 4f). Generally, a longer lifetime gives rise to a better transfer of photogenerated charge carriers for a semiconductor [64], leading to a higher solar energy conversion efficiency. However, this is not always the norm for a photocatalytic aerobic reaction because the different reduction

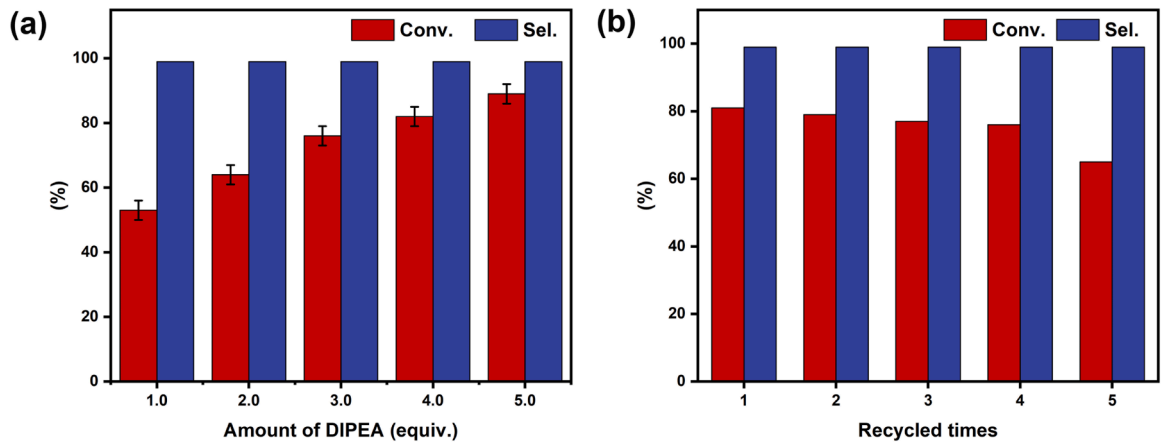


**Fig. 6.** (a) Influence of the amount of DIPEA on the blue light photocatalysis of EFC-CMP for aerobic hydroxylation of 2-phenyl-1,3,2-dioxaborinane to phenol. Reaction conditions: 2-phenyl-1,3,2-dioxaborinane (0.3 mmol), EFC-CMP (5 mg), blue LEDs (λ = 460 ± 10 nm), $C_2H_5OH$ (1 mL), air (1 atm), 1 h. (b) Recycle testing for blue light photocatalysis of EFC-CMP for aerobic hydroxylation of 2-phenyl-1,3,2-dioxaborinane to phenol. Reaction conditions: 2-phenyl-1,3,2-dioxaborinane (0.6 mmol), EFC-CMP (5 mg), DIPEA (5.0 equiv.), blue LEDs (λ = 460 ± 10 nm), $C_2H_5OH$ (5 mL), air (1 atm), 1 h. The conversion of 2-phenyl-1,3,2-dioxaborinane, and selectivity of phenol were determined by GC–FID using bromobenzene as the internal standard.

potentials and kinetics of TCB-CMP and EFC-CMP in reducing $O_2$ to $O_2^{\bullet-}$ might override the superiority given by a long lifetime of the charge carriers.

### 3.2. Hydroxylation of phenylboronic acids over carbazole-based CMPs

The hydroxylation of phenylboronic acids to phenols has garnered

**Table 1**
Blue light photocatalysis of EFC-CMP for aerobic hydroxylation of phenylboronic acids to phenols.[a].

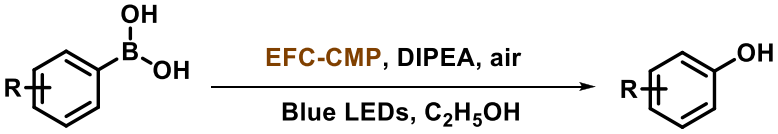


| Entry | Substrate | Product | *t* (h) | Yield (%)[b] |
|---|---|---|---|---|
| 1 | 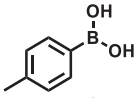 | 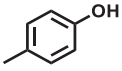 | 1.3 | 91 |
| 2 | 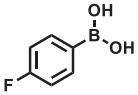 | 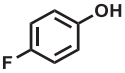 | 1.0 | 91 |
| 3 | 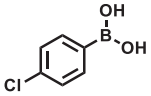 | 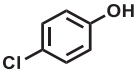 | 0.7 | 92 |
| 4 | 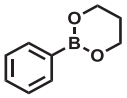 |  | 1.5 | 96 |
| 5 | 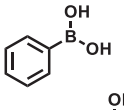 |  | 1.5 | 81 |
| 6 | 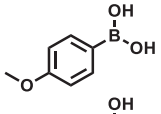 | 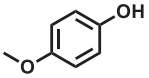 | 1.5 | 89 |
| 7 | 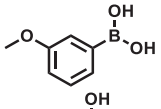 | 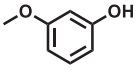 | 1.5 | 92 |
| 8 | 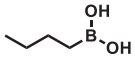 |  | 0.6 | 82 |
| 9 | 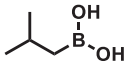 |  | 0.6 | 73 |

[a] Reaction conditions: boronic acid (0.6 mmol), EFC-CMP (5 mg), DIPEA (5.0 equiv.), blue LEDs (λ = 460 ± 10 nm), $C_2H_5OH$ (5 mL), air (1 atm).
[b] The yields of corresponding phenols for entries 1–4, 8, and 9 were determined by GC–FID using bromobenzene as the internal standard; and the yields of these for entries 5–7 were referring to isolated yields.

**Table 2**
Quenching experiments to determine the ROS for blue light photocatalysis of EFC-CMP for aerobic hydroxylation of 2-phenyl-1,3,2-dioxaborinane.[a].

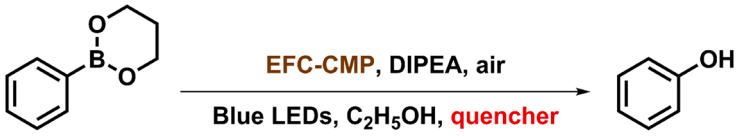


| Entry | Quencher (equiv.) | Roles | Conv. (%)[b] | Sel. (%)[b] |
|---|---|---|---|---|
| 1 | None | – | 63 | 99 |
| 2 | $N_2$ (–) | $O_2$ replacement | 0 | – |
| 3 | $K_2S_2O_8$ (1.0) | electron scavenger | 55 | 99 |
| 4 | *p*-BQ (0.3) | $O_2^{\bullet-}$ scavenger | 7 | 99 |

[a] Standard condition: 2-phenyl-1,3,2-dioxaborinane (0.6 mmol), EFC-CMP (5 mg), DIPEA (5.0 equiv.), blue LEDs ($\lambda = 460 \pm 10$ nm), $C_2H_5OH$ (5 mL), air (1 atm), 0.75 h.
[b] Determined by GC–FID using bromobenzene as the internal standard, conversion of 2-phenyl-1,3,2-dioxaborinane, selectivity of phenol.

much attention to assessing the activity of designed photocatalytic materials [65–69]. The porous property, excellent light-responsive capability, and outstanding transfer characteristics of interfacial charges for CMPs drive their distinct photocatalytic performance. Thus, the effectiveness of TCB-CMP and EFC-CMP were evaluated by blue light photocatalysis for aerobic hydroxylation of phenylboronic acids to phenols in the presence of $h^+$ quencher. However, considering phenylboronic acid is unstable during GC–FID analysis, 2-phenyl-1,3,2-dioxaborinane was synthesized via the esterification of phenylboronic acid to perform the blue light photocatalytic selective generation of phenol. Firstly, employing DIPEA as the $h^+$ quencher, the respective kinetic curves for aerobic hydroxylation of 2-phenyl-1,3,2-dioxaborinane to phenol in $C_2H_5OH$ have been acquired by blue light photocatalysis of EFC-CMP and TCB-CMP (Fig. 5) in which EFC-CMP exhibited superior performance to TCB-CMP. By contrast, the TCB and EFC monomers present no photocatalytic activity for aerobic hydroxylation of 2-phenyl-1,3,2-dioxaborinane to phenol in $C_2H_5OH$ (Supplementary Table S1).

Subsequently, a sequence of decisive factors affecting photocatalytic aerobic hydroxylation of 2-phenyl-1,3,2-dioxaborinane to phenols were screened to determine the optimal conditions, such as the choice for solvent, $h^+$ quencher and their dosage, light source, and so on. In $C_2H_5OH$, a decent conversion of 64% and the selectivity of 99% were obtained within 1 h over EFC-CMP during the blue light photocatalysis for aerobic hydroxylation of 2-phenyl-1,3,2-dioxaborinane to phenol (Supplementary Table S2). Switching the reaction solvent from $C_2H_5OH$ to $CH_3OH$, a more protic solvent, has a slightly negative effect on the formation of phenol. Notwithstanding that the superior conversion of 2-phenyl-1,3,2-dioxaborinane was delivered in $CH_3CN$, the obtained inferior selectivity of 85% propelled us to appoint $C_2H_5OH$ as the reliable solvent for the succeeding exploration. Then the amount of $C_2H_5OH$ was also investigated (Supplementary Table S3). Interestingly, the increase of the amount for $C_2H_5OH$ is conducive to the smooth proceeding for the reaction. Therefore 5 mL $C_2H_5OH$ was ascertained as the dosage of further experiments.

Afterward, the prestige of DIPEA in playing the role of $h^+$ quencher was validated by the comparison with triethylamine (TEA) (Supplementary Table S4). Likewise, the influence of the amount of DIPEA during the blue light photocatalysis of EFC-CMP for aerobic hydroxylation of 2-phenyl-1,3,2-dioxaborinane to phenol was administered (Fig. 6a). During the amount of DIPEA rising from 1.0 equiv. to 5.0 equiv., the incremental conversion for the protocol maintains a weakening trend but with high selectivity. When adopting 6.0 equiv. of DIPEA in the protocol, the conversion of 90% and the selectivity of 99% were acquired in 0.9 h. Considering the cost-effectiveness of experiments, 5.0 equiv. of DIPEA is more suitable for this protocol. Meantime, the evaluation about the influence of different wavelengths of LEDs on the visible light photocatalysis of EFC-CMP for aerobic hydroxylation of 2-phenyl-1,3,2-dioxaborinane to phenol was examined (Supplementary Fig. S9). Considering that a larger proportion in the visible light spectrum and the lower photon energy for blue light, the blue one is determined as the optimal choice for exciting EFC-CMP to participate in the photocatalytic aerobic hydroxylation of 2-phenyl-1,3,2-dioxaborinane to phenol. Besides, the light-emitting spectrum and intensity of the blue LED is supplied (Supplementary Fig. S10). Notably, the reusability test of EFC-CMP demonstrates that the photocatalytic activity of the recovered photocatalyst did not weaken markedly until the fifth cycle, attesting to the reusability and the robustness of EFC-CMP (Fig. 6b). Moreover, the robustness of TCB-CMP has also been proved, without significant decrease in photocatalytic activity for five cycles (Supplementary Fig. S11). Satisfactorily, all characteristic peaks in the FTIR spectra for recovered photocatalysts after five recycles remain intact (Supplementary Fig. S12), further suggesting the robustness of two carbazole-based CMPs.

### 3.3. Scope and mechanism of photocatalytic aerobic hydroxylation over EFC-CMP

To attest to the scope of substrates, an assortment of electronically diversified phenylboronic acids were subjected to blue light photocatalysis of EFC-CMP for selective generation of phenols with $O_2$ and DIPEA. Noteworthy, electron-withdrawing group substituted phenylboronic acids (Table 1, entries 2 and 3) are swifter to perform blue light photocatalytic aerobic hydroxylation than phenylboronic acids bearing electron-donating substituted group (Table 1, entry 1). Besides, the photocatalytic aerobic hydroxylation of 2-phenyl-1,3,2-dioxaborinane enabled by EFC-CMP could achieve a yield of 96% within 1.5 h upon the identical conditions (Table 1, entry 4). Meantime, the transformation of phenylboronic acid gave the target phenol a yield of 81% in the case of yield loss during the isolation (Table 1, entry 5). The result further confirms that the optimization strategy using 2-phenyl-1,3,2-dioxaborinane for blue light photocatalytic selective generation of phenol is reasonable. Also, the substituted position of $–OCH_3$ like *para*- or *meta*- position has no evident impact on the smooth proceeding of the reaction within the allowable range of error (Table 1, entries 6 and 7). Meanwhile, the photocatalytic strategy also could be applied to the aerobic hydroxylation of aliphatic boronic acid to corresponding alcohols under standard conditions (Table 1, entries 8 and 9). Overall, EFC-CMP possesses broad applicability for blue light photocatalytic aerobic hydroxylation of a series of phenylboronic acids to phenols and presents superior performance. Additionally, the ascendency of EFC-CMP on activity has been reflected as compared to other representative photocatalysts (Supplementary Table S5).

ROS plays a crucial role in determining the distribution of products and the reaction pathways. When the light, EFC-CMP, and DIPEA were respectively omitted from the protocol, the termination for reaction certifies that they are all indispensable (Supplementary Table S6). Meanwhile, quenching experiments were executed to ascertain the ROS

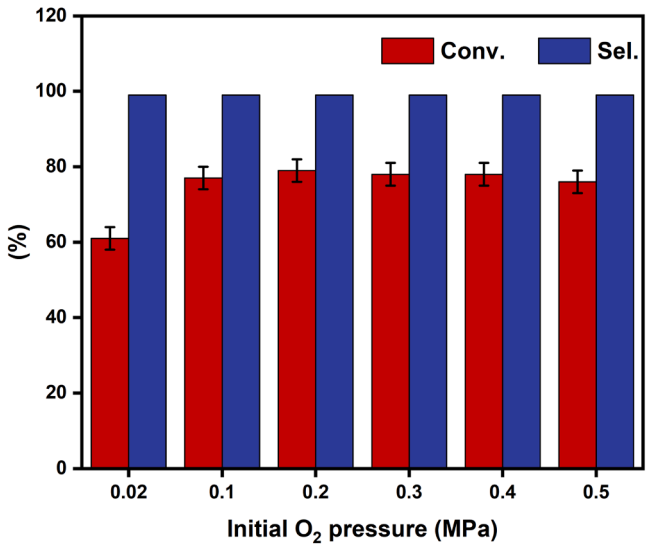


**Fig. 7.** Influence of initial $O_2$ pressure on aerobic hydroxylation of 2-phenyl-1,3,2-dioxaborinane to phenol by blue light photocatalysis of EFC-CMP. Reaction conditions: 2-phenyl-1,3,2-dioxaborinane (0.6 mmol), EFC-CMP (5 mg), DIPEA (5.0 equiv.), blue LEDs ($\lambda = 460 \pm 10$ nm), $C_2H_5OH$ (5 mL), 1 h. The conversion of 2-phenyl-1,3,2-dioxaborinane and selectivity of phenol were determined by GC–FID using bromobenzene as the internal standard.

involved in the blue light photocatalysis of EFC-CMP for aerobic hydroxylation of 2-phenyl-1,3,2-dioxaborinane to phenol (Table 2). Firstly, the aerobic hydroxylation of phenylboronic acids occurred in $C_2H_5OH$ that could quench any readily generated $^{\bullet}OH$. Therefore, one can rule out the role of $^{\bullet}OH$ in the reaction. In an atmosphere of $N_2$, no formation of phenol indicates that $O_2$ plays a crucial role in the transformation (Table 2, entries 1 and 2). Additionally, the introduction of $K_2S_2O_8$ could partially accept $e^-$ and therefore led to moderate curtailment in conversion (Table 2, entry 3). The results manifest that $e^-$ participates in the selective generation of phenol. Apparently, a negligible conversion was obtained after the addition of *p*-benzoquinone (*p*-BQ), disclosing that $O_2^{\bullet-}$ is the crucial ROS for this protocol (Table 2, entry 4). Usually, deuterated methanol ($CD_3OD$) is more accessible than deuterated ethanol, therefore the solvent was changed from $C_2H_5OH$ to $CH_3OH$ (Supplementary Table S7). The conversion in $CD_3OD$ was similar to the result given in $CH_3OH$, confirming that no singlet oxygen ($^1O_2$) is involved in the blue light photocatalysis of EFC-CMP for aerobic hydroxylation of 2-phenyl-1,3,2-dioxaborinane to phenol.

Next, the influence of initial pressure of $O_2$ on the blue light photocatalysis of EFC-CMP for aerobic hydroxylation of 2-phenyl-1,3,2-dioxaborinane to phenol was evaluated (Fig. 7). When the photocatalytic aerobic hydroxylation was transferred in 0.1 MPa $O_2$, the enhancement in conversion elucidates that an atmosphere of pure $O_2$ is more conducive to the smooth generation of phenol than the air. While the almost constant conversions subsequently were acquired, ranging from 0.1 MPa to 0.5 MPa for initial $O_2$ pressure. By and large, the impact of initial $O_2$ pressure is marginal on the aerobic hydroxylation of 2-phenyl-1,3,2-dioxaborinane over EFC-CMP.

Based on the preliminary verification for the existence of $O_2^{\bullet-}$ by the quenching experiments, a tentatively proposed mechanism is depicted in Fig. 8. Firstly, carbazole acting as the site of Lewis base could close the distance with the $-B(OH)_2$ group as Lewis acid. Secondly, the excited EFC-CMP, produced under the irradiation of blue LEDs, yields separated $e^-$ and $h^+$. Thirdly, the former further activates the adsorbed $O_2$ into $O_2^{\bullet-}$, and the generated $O_2^{\bullet-}$ would attack the vacant *p*-orbital of the electron-deficient boron center in **A** to form the peroxide radical intermediate **B**. Concurrently, $h^+$ is quenched by DIPEA and makes it transform to $DIPEA^{\bullet+}$, promoting the formation of phenol with a indirect role. Next, the intermediate **B** transforms to the unstable peroxide anion **C** by the abstraction of a proton from $DIPEA^{\bullet+}$, which would further be rearranged into phenyl dihydrogen orthoborate **D** through the removal of hydroxyl anion and the aryl migration. Ultimately, the hydrolysis of borate intermediate **D** affords the desired phenol **E**.

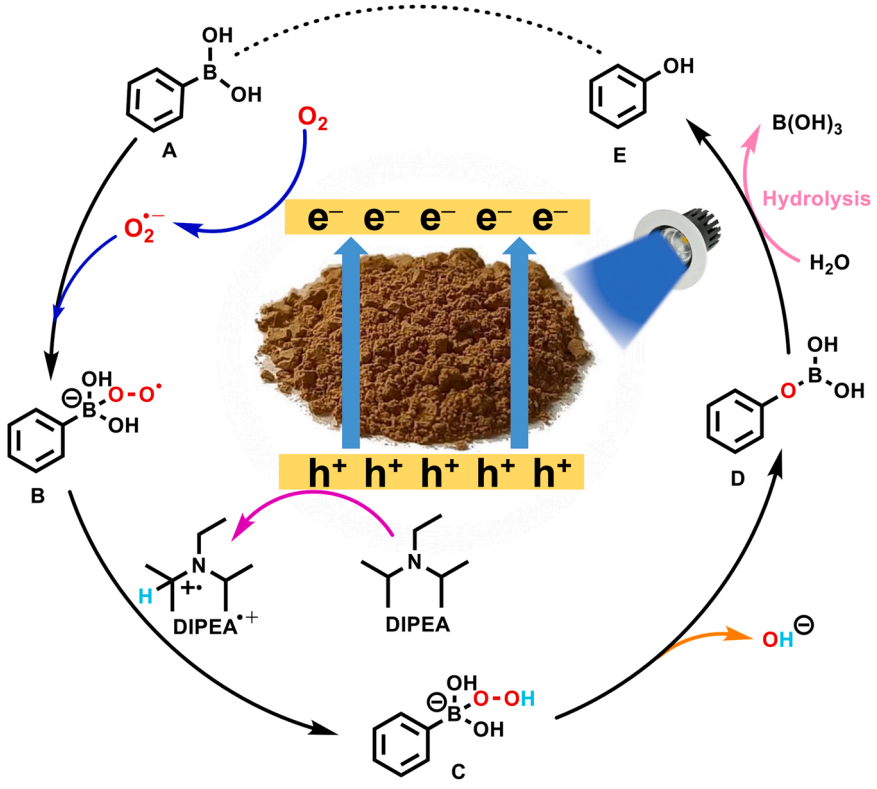


**Fig. 8.** The proposed mechanism of blue light photocatalysis of EFC-CMP for aerobic hydroxylation of phenylboronic acid to phenol.

## 4. Conclusions

In this work, two carbazole-based CMPs have been fabricated through C–C coupling polymerization. Gratifyingly, the blue light photocatalysis of both carbazole-based CMPs could execute the aerobic hydroxylation of phenylboronic acids in $C_2H_5OH$. Importantly, EFC-CMP imparted superior photocatalytic activity to TCB-CMP due to favorable generation of $e^-$. In this regime, carbazole acts as the site of Lewis base to close the distance with phenylboronic acids and donates $e^-$ for activating $O_2$ into $O_2^{\bullet-}$ to execute the hydroxylation of phenylboronic acids. Besides, $h^+$ (i.e., carbazole radical cation) interacts with DIPEA for alleviating the overoxidation of functionalized phenols, ensuring the highly selective generation of phenols in $C_2H_5OH$. The work demonstrates the feasibility of taming the oxidation potential of $h^+$ and the generation of $O_2^{\bullet-}$ through the selection of suitable building blocks of CMPs and regulating conditions in producing delicate products like phenols. The strategy could be furthered to implement new organic transformations and control the selectivity of products.

## CRediT authorship contribution statement

**Xiaoyun Dong**: Investigation, Writing – original draft. **Huimin Hao**: Investigation, Formal analysis. **Fulin Zhang**: Formal analysis. **Xianjun Lang**: Conceptualization, Supervision, Writing – review & editing, Funding acquisition.

## Declaration of Competing Interest

The authors declare that they have no known competing financial interests or personal relationships that could have appeared to influence the work reported in this paper.

## Acknowledgments

The financial support from the National Natural Science Foundation of China (Grants 22072108 and 21773173) is gratefully acknowledged.

## Appendix A. Supporting information

Supplementary data associated with this article can be found in the online version at doi:10.1016/j.apcatb.2022.121210.

## References

[1] R. Cannalire, S. Pelliccia, L. Sancineto, E. Novellino, G.C. Tron, M. Giustiniano, Visible light photocatalysis in the late-stage functionalization of pharmaceutically relevant compounds, Chem. Soc. Rev. 50 (2021) 766–897, https://doi.org/10.1039/d0cs00493f.

[2] X. Zhang, K.P. Rakesh, L. Ravindar, H.L. Qin, Visible-light initiated aerobic oxidations: A critical review, Green Chem. 20 (2018) 4790–4833, https://doi.org/10.1039/c8gc02382d.

[3] C.X. Yuan, A.M. Eliasen, A.M. Camelio, D. Siegel, Preparation of phenols by phthaloyl peroxide-mediated oxidation of arenes, Nat. Protoc. 9 (2014) 2624–2629, https://doi.org/10.1038/nprot.2014.175.

[4] S. Quideau, D. Deffieux, C. Douat-Casassus, L. Pouységu, Plant polyphenols: Chemical properties, biological activities, and synthesis, Angew. Chem. Int. Ed. 50 (2011) 586–621, https://doi.org/10.1002/anie.201000044.

[5] L. Cheng, H.H. Wang, H.R. Cai, J. Zhang, X. Gong, W. Han, Iron-catalyzed arene C−H hydroxylation, Science 374 (2021) 77–81, https://doi.org/10.1126/science.abj0731.

[6] S. Fukuzumi, K. Doi, A. Itoh, T. Suenobu, K. Ohkubo, Y. Yamada, K.D. Karlin, Formation of a long-lived electron-transfer state in mesoporous silica-alumina composites enhances photocatalytic oxygenation reactivity, Proc. Natl. Acad. Sci. U.S.A. 109 (2012) 15572–15577, https://doi.org/10.1073/pnas.1119994109.

[7] J.A. Johnson, J. Luo, X. Zhang, Y.S. Chen, M.D. Morton, E. Echeverria, F.E. Torres, J. Zhang, Porphyrin-metalation-mediated tuning of photoredox catalytic properties in metal-organic frameworks, ACS Catal. 5 (2015) 5283–5291, https://doi.org/10.1021/acscatal.5b00941.

[8] J.J. Molloy, T.A. Clohessy, C. Irving, N.A. Anderson, G.C. Lloyd-Jones, A.J. B. Watson, Chemoselective oxidation of aryl organoboron systems enabled by boronic acid-selective phase transfer, Chem. Sci. 8 (2017) 1551–1559, https://doi.org/10.1039/c6sc04014d.

[9] M. Karthik, P. Suresh, Graphene oxide as a carbocatalyst for sustainable *ipso*-hydroxylation of arylboronic acids: A simple and straightforward strategy to access phenols, ACS Sustainable Chem. Eng. 7 (2019) 9028–9034, https://doi.org/10.1021/acssuschemeng.9b01361.

[10] K.X. Wang, M. Tong, Y.N. Yang, B.Y. Zhang, H.L. Liu, H.X. Li, F. Zhang, Visible light-catalytic hydroxylation of aryl halides with water to phenols by carbon nitride and nickel complex cooperative catalysis, Green Chem. 22 (2020) 7417–7423, https://doi.org/10.1039/d0gc02367a.

[11] T. Toyao, N. Ueno, K. Miyahara, Y. Matsui, T.H. Kim, Y. Horiuchi, H. Ikeda, M. Matsuoka, Visible-light, photoredox catalyzed, oxidative hydroxylation of arylboronic acids using a metal-organic framework containing tetrakis (carboxyphenyl)porphyrin groups, Chem. Commun. 51 (2015) 16103–16106, https://doi.org/10.1039/c5cc06163f.

[12] X. Yu, S.M. Cohen, Photocatalytic metal-organic frameworks for the aerobic oxidation of arylboronic acids, Chem. Commun. 51 (2015) 9880–9883, https://doi.org/10.1039/c5cc01697e.

[13] D.P. Luo, Y.F. Huang, X.Y. Hong, D.B. Chen, G.X. Li, X.B. Huang, W.X. Gao, M. C. Liu, Y.B. Zhou, H.Y. Wu, Phthalocyanine zinc-catalyzed hydroxylation of aryl boronic acids under visible light, Adv. Synth. Catal. 361 (2019) 961–964, https://doi.org/10.1002/adsc.201801276.

[14] Y. Nosaka, A.Y. Nosaka, Generation and detection of reactive oxygen species in photocatalysis, Chem. Rev. 117 (2017) 11302–11336, https://doi.org/10.1021/acs.chemrev.7b00161.

[15] J. Schneider, M. Matsuoka, M. Takeuchi, J.L. Zhang, Y. Horiuchi, M. Anpo, D. W. Bahnemann, Understanding $TiO_2$ photocatalysis: Mechanisms and materials, Chem. Rev. 114 (2014) 9919–9986, https://doi.org/10.1021/cr5001892.

[16] P. Lyu, J. Zhu, C.C. Han, L. Qiang, L.L. Zhang, B.B. Mei, J.H. He, X.Y. Liu, Z.F. Bian, H.X. Li, Self-driven reactive oxygen species generation via interfacial oxygen vacancies on carbon-coated $TiO_{2-x}$ with versatile applications, ACS Appl. Mater. Interfaces 13 (2021) 2033–2043, https://doi.org/10.1021/acsami.0c19414.

[17] W.P. Zhang, G.Y. Li, H.L. Liu, J.Y. Chen, S.T. Ma, M.C. Wen, J.J. Kong, T.C. An, Photocatalytic degradation mechanism of gaseous styrene over Au/$TiO_2$@CNTs: Relevance of superficial state with deactivation mechanism, Appl. Catal., B 272 (2020) 118969, https://doi.org/10.1016/j.apcatb.2020.118969.

[18] J.Y. Chen, Z.L. Zhang, W.K. Zhu, L.Y. Zhang, B.C. Zhao, Y.M. Ji, G.Y. Li, T.C. An, Superoxide radical enhanced photocatalytic performance of styrene alters its degradation mechanism and intermediate health risk on $TiO_2$/graphene surface, Environ. Res. 195 (2021) 110747, https://doi.org/10.1016/j.envres.2021.110747.

[19] M.H. Muhammad, X.L. Chen, Y. Liu, T. Shi, Y.Y. Peng, L.B. Qu, B. Yu, Recyclable Cu@$C_3N_4$-catalyzed hydroxylation of aryl boronic acids in water under visible light: Synthesis of phenols under ambient conditions and room temperature, ACS Sustainable Chem. Eng. 8 (2020) 2682–2687, https://doi.org/10.1021/acssuschemeng.9b06010.

[20] I. Kumar, R. Sharma, R. Kumar, R. Kumar, U. Sharma, $C_{70}$ fullerene-catalyzed metal-free photocatalytic *ipso*-hydroxylation of aryl boronic acids: Synthesis of phenols, Adv. Synth. Catal. 360 (2018) 2013–2019, https://doi.org/10.1002/adsc.201701573.

[21] F. Parrino, M. Bellardita, E.I. García-López, G. Marcì, V. Loddo, L. Palmisano, Heterogeneous photocatalysis for selective formation of high-value-added molecules: Some chemical and engineering aspects, ACS Catal. 8 (2018) 11191–11225, https://doi.org/10.1021/acscatal.8b03093.

[22] K. Mori, M. Kawashima, M. Che, H. Yamashita, Enhancement of the photoinduced oxidation activity of a ruthenium(II) complex anchored on silica-coated silver nanoparticles by localized surface plasmon resonance, Angew. Chem. Int. Ed. 49 (2010) 8598–8601, https://doi.org/10.1002/anie.201004942.

[23] D.T. Sawyer, J.S. Valentine, How super is superoxide? Acc. Chem. Res. 14 (1981) 393–400, https://doi.org/10.1021/ar00072a005.

[24] I. Grčić, N. Koprivanac, G. Li Puma, Modeling the photocatalytic oxidation of carboxylic acids on aqueous $TiO_2$ suspensions and on immobilized $TiO_2$-chitosan thin films in different reactor geometries irradiated by UVA or UVC light sources, Chem. Eng. J. 422 (2021) 130104, https://doi.org/10.1016/j.cej.2021.130104.

[25] S.X. Yang, X. Li, Y. Qin, Y. Cheng, W.W. Fan, X.J. Lang, L.Y. Zheng, Q.E. Cao, Modulating the stacking model of covalent organic framework isomers with different generation efficiencies of reactive oxygen species, ACS Appl. Mater. Interfaces 13 (2021) 29471–29481, https://doi.org/10.1021/acsami.1c03170.

[26] X.S. Ding, B.H. Han, Metallophthalocyanine-based conjugated microporous polymers as highly efficient photosensitizers for singlet oxygen generation, Angew. Chem. Int. Ed. 54 (2015) 6536–6539, https://doi.org/10.1002/anie.201501732.

[27] J.L. Shi, R.F. Chen, H.M. Hao, C. Wang, X.J. Lang, 2D $sp^2$ carbon-conjugated porphyrin covalent organic framework for cooperative photocatalysis with TEMPO, Angew. Chem. Int. Ed. 59 (2020) 9088–9093, https://doi.org/10.1002/anie.202000723.

[28] P. Kong, H. Tan, T.Y. Lei, J. Wang, W.J. Yan, R.Y. Wang, E.R. Waclawik, Z. F. Zheng, Z. Li, Oxygen vacancies confined in conjugated polyimide for promoted visible-light photocatalytic oxidative coupling of amines, Appl. Catal., B 272 (2020) 118964, https://doi.org/10.1016/j.apcatb.2020.118964.

[29] X. Li, H.M. Hao, X.J. Lang, Thiazolo[5,4-*d*]thiazole linked conjugated microporous polymer photocatalysis for selective aerobic oxidation of amines, J. Colloid Interface Sci. 593 (2021) 380–389, https://doi.org/10.1016/j.jcis.2021.02.111.

[30] L. Ma, Y.L. Liu, Y. Liu, S.Y. Jiang, P. Li, Y.C. Hao, P.P. Shao, A.X. Yin, X. Feng, B. Wang, Ferrocene-linkage-facilitated charge separation in conjugated microporous polymers, Angew. Chem. Int. Ed. 58 (2019) 4221–4226, https://doi.org/10.1002/anie.201813598.

[31] C.Y. Song, J.Q. Nie, C. Ma, C.F. Lu, F.Y. Wang, G.C. Yang, 1,2,3-Triazole-based conjugated porous polymers for visible light induced oxidative organic

transformations, Appl. Catal. B 287 (2021), 119984, https://doi.org/10.1016/j.apcatb.2021.119984.
[32] B. Liang, H. Wang, X.H. Shi, B.Y. Shen, X. He, Z.A. Ghazi, N.A. Khan, H. Sin, A. M. Khattak, L.S. Li, Z.Y. Tang, Microporous membranes comprising conjugated polymers with rigid backbones enable ultrafast organic-solvent nanofiltration, Nat. Chem. 10 (2018) 961–967, https://doi.org/10.1038/s41557-018-0093-9.
[33] G.G. Zhang, Z.A. Lan, X.C. Wang, Conjugated polymers: Catalysts for photocatalytic hydrogen evolution, Angew. Chem. Int. Ed. 55 (2016) 15712–15727, https://doi.org/10.1002/anie.201607375.
[34] W.H. Sun, Y.G. Xiang, Z.H. Jiang, S.Y. Wang, N. Yang, S.B. Jin, L.H. Sun, H.L. Teng, H. Chen, Designed polymeric conjugation motivates tunable activation of molecular oxygen in heterogeneous organic photosynthesis, Sci. Bull. 67 (2022) 61–70, https://doi.org/10.1016/j.scib.2021.07.016.
[35] R.S. Sprick, B. Bonillo, R. Clowes, P. Guiglion, N.J. Brownbill, B.J. Slater, F. Blanc, M.A. Zwijnenburg, D.J. Adams, A.I. Cooper, Visible-light-driven hydrogen evolution using planarized conjugated polymer photocatalysts, Angew. Chem. Int. Ed. 55 (2016) 1824–1828, https://doi.org/10.1002/anie.201510542.
[36] T. Zhang, G.L. Xing, W.B. Chen, L. Chen, Porous organic polymers: A promising platform for efficient photocatalysis, Mater. Chem. Front. 4 (2020) 332–353, https://doi.org/10.1039/c9qm00633h.
[37] G.Q. Zhang, W. Ou, J. Wang, Y.S. Xu, D. Xu, T. Sun, S.N. Xiao, M.R. Wang, H.X. Li, W. Chen, C.L. Su, Stable, carrier separation tailorable conjugated microporous polymers as a platform for highly efficient photocatalytic $H_2$ evolution, Appl. Catal., B 245 (2019) 114–121, https://doi.org/10.1016/j.apcatb.2018.12.007.
[38] X. Li, X.M. Ma, F.L. Zhang, X.Y. Dong, X.J. Lang, Selective photocatalytic formation of sulfoxides by aerobic oxidation of sulfides over conjugated microporous polymers with thiazolo[5,4-*d*]thiazole linkage, Appl. Catal., B 298 (2021) 120514, https://doi.org/10.1016/j.apcatb.2021.120514.
[39] J. Xiao, X.L. Liu, L. Pan, C.X. Shi, X.W. Zhang, J.J. Zou, Heterogeneous photocatalytic organic transformation reactions using conjugated polymers-based materials, ACS Catal. 10 (2020) 12256–12283, https://doi.org/10.1021/acscatal.0c03480.
[40] H. Yamashita, K. Mori, Y. Kuwahara, T. Kamegawa, M.C. Wen, P. Verma, M. Che, Single-site and nano-confined photocatalysts designed in porous materials for environmental uses and solar fuels, Chem. Soc. Rev. 47 (2018) 8072–8096, https://doi.org/10.1039/c8cs00341f.
[41] Q. Chen, M. Luo, P. Hammershoj, D. Zhou, Y. Han, B.W. Laursen, C.G. Yan, B. H. Han, Microporous polycarbazole with high specific surface area for gas storage and separation, J. Am. Chem. Soc. 134 (2012) 6084–6087, https://doi.org/10.1021/ja300438w.
[42] J. Luo, X. Zhang, J. Zhang, Carbazolic porous organic framework as an efficient, metal-free visible-light photocatalyst for organic synthesis, ACS Catal. 5 (2015) 2250–2254, https://doi.org/10.1021/acscatal.5b00025.
[43] M.L. Yang, I.S. Park, T. Yasuda, Full-color, narrowband, and high-efficiency electroluminescence from boron and carbazole embedded polycyclic heteroaromatics, J. Am. Chem. Soc. 142 (2020) 19468–19472, https://doi.org/10.1021/jacs.0c10081.
[44] C.L. Su, R. Tandiana, B.B. Tian, A. Sengupta, W. Tang, J. Su, K.P. Loh, Visible-light photocatalysis of aerobic oxidation reactions using carbazolic conjugated microporous polymers, ACS Catal. 6 (2016) 3594–3599, https://doi.org/10.1021/acscatal.6b00443.
[45] T.L. Lee, A.M. Elewa, M.G. Kotp, H.H. Chou, A.F.M. El-Mahdy, Carbazole- and thiophene-containing conjugated microporous polymers with different planarity for enhanced photocatalytic hydrogen evolution, Chem. Commun. 57 (2021) 11968–11971, https://doi.org/10.1039/d1cc04551b.
[46] Q.J. Xie, Y.M. Yang, W.J. Zhang, Z. Gao, X.F. Li, J.T. Tang, C.Y. Pan, G.P. Yu, Polarization-induced charge separation in conjugated microporous polymers for efficient visible light-driven C-3 selenocyanation of indoles, Chem. Sci. 12 (2021) 5631–5637, https://doi.org/10.1039/d0sc06951e.
[47] Y.F. Zhi, Z.J. Yao, W.B. Jiang, H. Xia, Z. Shi, Y. Mu, X.M. Liu, Conjugated microporous polymers as heterogeneous photocatalysts for efficient degradation of a mustard-gas simulant, ACS Appl. Mater. Interfaces 11 (2019) 37578–37585, https://doi.org/10.1021/acsami.9b10958.
[48] Y.F. Zhi, S. Ma, H. Xia, Y.M. Zhang, Z. Shi, Y. Mu, X.M. Liu, Construction of donor-acceptor type conjugated microporous polymers: A fascinating strategy for the development of efficient heterogeneous photocatalysts in organic synthesis, Appl. Catal., B 244 (2019) 36–44, https://doi.org/10.1016/j.apcatb.2018.11.032.
[49] L.P. Guo, Y.L. Niu, S. Razzaque, B. Tan, S.B. Jin, Design of D–$A_1$–$A_2$ covalent triazine frameworks via copolymerization for photocatalytic hydrogen evolution, ACS Catal. 9 (2019) 9438–9445, https://doi.org/10.1021/acscatal.9b01951.
[50] L.P. Guo, Y.L. Niu, H.T. Xu, Q.W. Li, S. Razzaque, Q. Huang, S.B. Jin, B. Tan, Engineering heteroatoms with atomic precision in donor–acceptor covalent triazine frameworks to boost photocatalytic hydrogen production, J. Mater. Chem. A 6 (2018) 19775–19781, https://doi.org/10.1039/c8ta07391k.
[51] Z.Z. Yang, H. Chen, B. Li, W. Guo, K.C. Jie, Y.F. Sun, D.E. Jiang, I. Popovs, S. Dai, Topotactic synthesis of phosphabenzene-functionalized porous organic polymers: Efficient ligands in $CO_2$ conversion, Angew. Chem. Int. Ed. 58 (2019) 13763–13767, https://doi.org/10.1002/anie.201907015.
[52] Y. Yuan, H.L. Huang, L. Chen, Y.L. Chen, *N,N′*-Bicarbazole: A versatile building block toward the construction of conjugated porous polymers for $CO_2$ capture and dyes adsorption, Macromolecules 50 (2017) 4993–5003, https://doi.org/10.1021/acs.macromol.7b00971.
[53] C. Gu, N. Huang, J. Gao, F. Xu, Y.H. Xu, D.L. Jiang, Controlled synthesis of conjugated microporous polymer films: Versatile platforms for highly sensitive and label-free chemo- and biosensing, Angew. Chem. Int. Ed. 53 (2014) 4850–4855, https://doi.org/10.1002/anie.201402141.
[54] C. Gu, N. Huang, Y.C. Chen, L.Q. Qin, H. Xu, S.T. Zhang, F.H. Li, Y.G. Ma, D. L. Jiang, π-Conjugated microporous polymer films: Designed synthesis, conducting properties, and photoenergy conversions, Angew. Chem. Int. Ed. 54 (2015) 13594–13598, https://doi.org/10.1002/anie.201506570.
[55] S.H. Xiong, X. Tang, C.Y. Pan, L. Li, J.T. Tang, G.P. Yu, Carbazole-bearing porous organic polymers with a mulberry-like morphology for efficient iodine capture, ACS Appl. Mater. Interfaces 11 (2019) 27335–27342, https://doi.org/10.1021/acsami.9b07679.
[56] C.X. Zhao, Z.P. Chen, R. Shi, X.F. Yang, T.R. Zhang, Recent advances in conjugated polymers for visible-light-driven water splitting, Adv. Mater. 32 (2020) 1907296, https://doi.org/10.1002/adma.201907296.
[57] D. Spasiano, R. Marotta, S. Malato, P. Fernandez-Ibañez, I. Di Somma, Solar photocatalysis: Materials, reactors, some commercial, and pre-industrialized applications. A comprehensive approach, Appl. Catal., B 170 (2015) 90–123, https://doi.org/10.1016/j.apcatb.2014.12.050.
[58] X.G. Meng, L.Q. Liu, S.X. Ouyang, H. Xu, D.F. Wang, N.Q. Zhao, J.H. Ye, Nanometals for solar-to-chemical energy conversion: From semiconductor-based photocatalysis to plasmon-mediated photocatalysis and photo-thermocatalysis, Adv. Mater. 28 (2016) 6781–6803, https://doi.org/10.1002/adma.201600305.
[59] M.J. Yu, W.W. Zhang, Z.Q. Guo, Y.Z. Wu, W.H. Zhu, Engineering nanoparticulate organic photocatalysts via a scalable flash nanoprecipitation process for efficient hydrogen production, Angew. Chem. Int. Ed. 60 (2021) 15590–15597, https://doi.org/10.1002/anie.202104233.
[60] J. Luo, J.Z. Lu, J. Zhang, Carbazole-triazine based donor-acceptor porous organic frameworks for efficient visible-light photocatalytic aerobic oxidation reactions, J. Mater. Chem. A 6 (2018) 15154–15161, https://doi.org/10.1039/c8ta05329d.
[61] H. Xu, X. Li, H.M. Hao, X.Y. Dong, W.L. Sheng, X.J. Lang, Designing fluorene-based conjugated microporous polymers for blue light-driven photocatalytic selective oxidation of amines with oxygen, Appl. Catal., B 285 (2021) 119796, https://doi.org/10.1016/j.apcatb.2020.119796.
[62] X.Y. Dong, H. Xu, H.M. Hao, W.L. Sheng, X.J. Lang, Selective photocatalytic oxidation of sulfides with dioxygen over carbazole-fluorene conjugated microporous polymers, J. Colloid Interface Sci. 608 (2022) 882–892, https://doi.org/10.1016/j.jcis.2021.10.047.
[63] W.R. Leow, J.C. Yu, B. Li, B.H. Hu, W. Li, X.D. Chen, Correlating the surface basicity of metal oxides with photocatalytic hydroxylation of boronic acids to alcohols, Angew. Chem. Int. Ed. 57 (2018) 9780–9784, https://doi.org/10.1002/anie.201805395.
[64] Z.W. Jin, M.J. Yuan, H. Li, H. Yang, Q. Zhou, H.B. Liu, X.Z. Lan, M.X. Liu, J. Z. Wang, E.H. Sargent, Y.L. Li, Graphdiyne: An efficient hole transporter for stable high-performance colloidal quantum dot solar cells, Adv. Funct. Mater. 26 (2016) 5284–5289, https://doi.org/10.1002/adfm.201601570.
[65] L.M. Sun, R. Li, W.W. Zhan, Y.S. Yuan, X.J. Wang, X.G. Han, Y.L. Zhao, Double-shelled hollow rods assembled from nitrogen/sulfur-codoped carbon coated indium oxide nanoparticles as excellent photocatalysts, Nat. Commun. 10 (2019) 2270, https://doi.org/10.1038/s41467-019-10302-0.
[66] J.K. Jin, K. Wu, X.Y. Liu, G.Q. Huang, Y.L. Huang, D. Luo, M. Xie, Y.F. Zhao, W. G. Lu, X.P. Zhou, J. He, D. Li, Building a pyrazole–benzothiadiazole–pyrazole photosensitizer into metal–organic frameworks for photocatalytic aerobic oxidation, J. Am. Chem. Soc. 143 (2021) 21340–21349, https://doi.org/10.1021/jacs.1c10008.
[67] P.F. Wei, M.Z. Qi, Z.P. Wang, S.Y. Ding, W. Yu, Q. Liu, L.K. Wang, H.Z. Wang, W. K. An, W. Wang, Benzoxazole-linked ultrastable covalent organic frameworks for photocatalysis, J. Am. Chem. Soc. 140 (2018) 4623–4631, https://doi.org/10.1021/jacs.8b00571.
[68] B.H. Tang, W.Q. Xu, J.F. Xu, X. Zhang, Transforming a fluorochrome to an efficient photocatalyst for oxidative hydroxylation: A supramolecular dimerization strategy based on host-enhanced charge transfer, Angew. Chem. Int. Ed. 60 (2021) 9384–9388, https://doi.org/10.1002/anie.202100185.
[69] Y.Y. Qan, D.D. Li, Y.L. Han, H.L. Jiang, Photocatalytic molecular oxygen activation by regulating excitonic effects in covalent organic frameworks, J. Am. Chem. Soc. 142 (2020) 20763–20771, https://doi.org/10.1021/jacs.0c09727.